Characterization of radiation damage induced by B and B_4 ion implantation into silicon

J.H. Liang [a,b,*], Y.Z. Chen [a], C.M. Lin [c]

[a] Institute of Nuclear Engineering and Science, National Tsing Hua University, Hsinchu 300, Taiwan, ROC
[b] Department of Engineering and System Science, National Tsing Hua University, Hsinchu 300, Taiwan, ROC
[c] Department of Applied Science, National Hsinchu University of Education, Hsinchu 300, Taiwan, ROC

ABSTRACT

In this study, B_1^- monomer and B_4^- cluster ions of the same boron kinetic energy level per atom (20 keV/atom) and total atomic fluence (2×10^{15} atoms/cm²) were implanted into silicon wafers held at liquid nitrogen temperature (LT, -196 °C), and followed by a two-step furnace annealing together with rapid thermal annealing treatment. The characteristics of radiation damage in both the as-implanted and as-annealed specimens were probed using Raman scattering spectroscopy (RSS) as well as transmission electron microscopy (TEM). Both the RSS and TEM results revealed that heavily-damaged and amorphous structures are formed in the as-implanted B_1 and B_4 specimens, respectively, mainly due to the so-called non-linear damage effect existed in the latter. Furthermore, there is less radiation damage remained in the as-annealed B_4 specimens when compared to the as-annealed B_1 ones, resulting from the occurrence of solid phase epitaxial growth (SPEG) in the amorphous layer of the former which thus causes significant removal of radiation damage.

© 2011 Elsevier B.V. All rights reserved.

1. Introduction

Recently, the evolution of scaled-down modern micro-electronic devices has imposed considerable challenges for low-energy ion implantation technologies in fabricating shallow junctions [1]. However, the fact that the extracted ion beam current decreases drastically at low ion energy levels has seriously restricted the direct use of low-energy ion implantation to meet the needs [2]. Among many proposed alternatives, B_n cluster ion implantation has received growing interest due to its superior advantages, especially when compared to boron monomer ion implantation under the same boron kinetic energy level per atom. These advantages includes [3–8]: (1) an $n^{5/2}$ amplification factor for beam transport gain which considerably increases the extracted ion beam current; (2) a $1/n$ reduction factor for implantation time which greatly reduces implantation costs; and (3) a non-linear ($>n$) superposition factor for radiation damage which significantly suppresses the ion channeling effect.

As mentioned above, radiation damage produced by a cluster ion is greater than a linear superposition of the radiation damage produced by the individual ions in the cluster ion (i.e. the so-called the non-linear damage effect) [9,10]. The non-linear damage effect is of prime importance, especially in the formation of shallow junc-

tions, due to the fact that the damage-dependent effects of such as ion channeling and transient-enhanced diffusion (TED) [11,12] may extend boron depth profiles into the bulk. In essence, the effects of ion channeling and TED tend to decrease and increase, respectively, as radiation damage increases. However, when the amount of radiation damage is enormous enough to form a sufficiently-thick amorphous layer, the occurrence of solid phase epitaxial growth (SPEG) [3,13] in the amorphous layer during the low-temperature post-annealing treatment will cause significant removal of radiation damage and subsequently lessen the TED effect. Therefore, a thorough understanding of the behavior of radiation damage produced by B_n cluster ion implantation prior to its industrial applications is crucial and is the central objective of this study. Furthermore, the amount of radiation damage strongly depends on implantation temperature due to the in situ annealing effect during ion implantation [14–16]. Hence, this study employs ion implantation at liquid nitrogen temperature (LT) in order to conceivably exclude the implantation temperature effect when quantitatively identifying how cluster size (i.e. n, the number of cluster constituents) affects the characteristics of radiation damage. Notably, B_4^- cluster ion implantation is adopted in this study to represent the B_n cluster ion implantations while B_1^- monomer ion implantation is adopted for making comparisons. In addition, this study employs the widely-used two-step method to carry out post-annealing treatments [17,18] in which an attempt is made to effectively (1) repair radiation damage during the first furnace annealing (FA) step at low temperatures and (2) activate the

implanted boron atoms during the second rapid thermal annealing (RTA) step at high temperatures.

2. Experimental details

In this study, 2×2 cm square specimens were deliberately prepared from Czochralski-grown n-type Si < 100 > wafers (3–7 Ω-cm). The specimens, held at LT by a flux of liquid nitrogen passing beneath the target holder, were implanted with B_1^- and B_4^- ions individually under the same boron kinetic energy level per atom of 20 keV/atom (i.e. 20 and 77 keV implantation energy levels for B_1^- and B_4^-, respectively) and total atom fluence (Φ) of 2×10^{15} atoms/cm^2 (i.e. 2×10^{15} and 5×10^{14} ions/cm^2 implantation fluences for B_1^- and B_4^-, respectively). The unit "cm^{-2}" is used hereafter to represent "atoms/cm^2" for simplicity. All of the ion implantations were carried out using the low-energy beam line of a NEC 9SDH-2 3MV tandem accelerator. Notably, 77 keV is the highest kinetic energy that can be obtained from the low-energy beam line and was thus adopted in this study as the implantation energy for B_4^- ions to approximate 20 keV/atom. Also, the specimens were tilted at an angle of 7° with respect to the incident ion beam in order to minimize the ion channeling effect. The implanted area on the specimens was 1.5 cm in diameter.

Following implantation, the as-implanted specimens underwent two-step post-annealing treatments. The first step involved the furnace annealing (FA) method using a Lindberg FA system (in nitrogen ambient) at 550 °C for 3 h. The second step involved the rapid thermal annealing (RTA) method using a Heatpulse 610 RTA system (in nitrogen ambient) at 1050 °C for 25 s.

All of the non-implanted, as-implanted, and as-annealed specimens were measured using Raman scattering spectroscopy (RSS) in order to probe the characteristics of radiation damage. In the measurements, the Raman spectra were room-temperature recorded by means of a micro-Raman spectrometer together with a triple grating mono-chromator (TRIAX 550) in backscattering geometry. The detection time was 20 s with a step size of 1.2 cm^{-1} in wavenumber. Notably, the penetration depth of the argon laser beam (wavelength = 514.5 nm) in silicon can be well estimated by its absorption coefficient in silicon and is approximately 762 nm [19], indicating that the detected depth is sufficient to cover the entire radiation damage region under investigation. Furthermore, cross-sectional transmission electron microscopy (XTEM) as well as plan-view transmission electron microscopy (PTEM) were utilized to identify the microstructures of radiation damage in both the as-implanted and as-annealed specimens. Both XTEM and PTEM observations were made via a JEOL-2000 FX II transmission electron microscope using an acceleration voltage of 200 kV.

3. Results and discussion

Fig. 1 shows the calculated depth profiles of boron atoms, displaced silicon atoms, net defects, and total defects due to 2×10^{15} cm^{-2} B_1 monomer ion implantation using the SRIM simulation code [20], where net defects denote the net amount of defects (i.e. interstitials minus vacancies) and total defects represent the total amount of defects (i.e. interstitials plus vacancies). As can be seen, the features of those depth profiles can be summarized as follows: (1) the average range (R_p), longitudinal range straggling (ΔR_p), skewness (γ), and kurtosis (β) are, respectively, 74.6 nm, 28.0 nm, −0.26, and 2.6 for the depth profile of boron atoms; and 53.3 nm, 28.0 nm, 0.23, and 2.3 for the depth profile of displaced silicon atoms; (2) the amount of displaced silicon atoms (i.e. excess self-interstitials) is much greater than that of implanted boron atoms; (3) the depth profile of net defects consists of three separate regions (i.e. vacancy-rich, neutral, and inter-
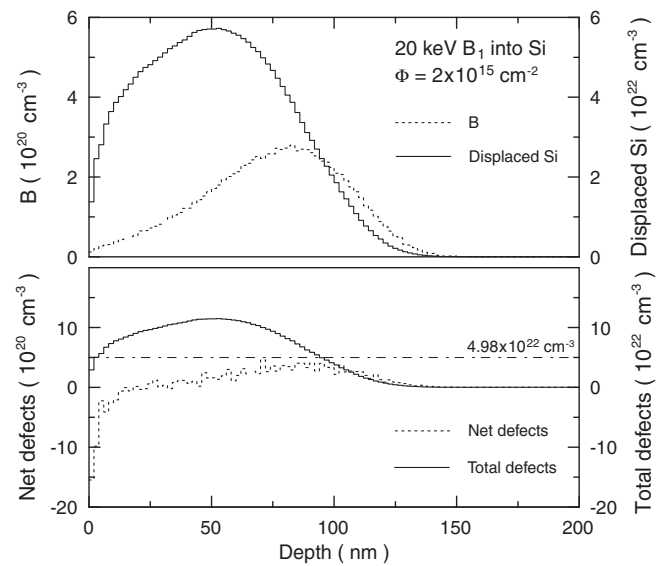

Fig. 1. SRIM-calculated depth profiles of boron atoms, net defects, displaced silicon atoms, and total defects in the as-implanted specimen with 2×10^{15} cm^{-2}, 20 keV B_1 monomer ion implantation.

stitial-rich) located consecutively from the specimen surface to the bulk; (4) the average ranges of the vacancy-rich ($\bar{x}_v$), neutral ($\bar{x}_n$), and interstitial-rich ($\bar{x}_i$) regions are 5.5, 23.4, and 84.1 nm, respectively; (5) the end-of-range (EOR) defects (primarily displaced silicon atoms), located around the amorphous-to-crystalline (a/c) interface (i.e. in the interstitial-rich region), are the main factor responsible for the TED effect when annealed [11]; (6) the depth profile of total defects is highly skewed and lies closer to the specimen surface in contrast to those of boron and displaced silicon atoms; (7) the depth profile of total defects spans from the specimen surface to approximately 158 nm with a broad peak at 54 nm; and (8) the locations at which the concentration of total defects equals the atomic number density of silicon (i.e. 4.98×10^{22} cm^{-3} [21]) lie between 5.0 and 95.8 nm, corresponding to an amorphous layer thickness of 90.8 nm.

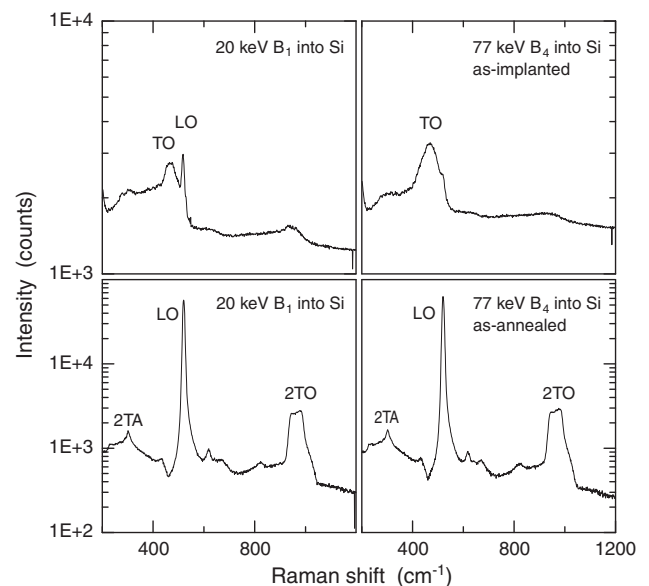**Fig. 2.** Raman spectra in the as-implanted (top) and as-annealed (bottom) specimens with 2×10^{15} cm^{-2}, 20 keV/atom B_1 monomer (left) and B_4 cluster (right) ion implantations.

Table 1
I_0 and FWHM of the LO and TO Raman characteristic peaks in the non-implanted, as-implanted, as-annealed specimens with 2×10^{15} cm^{-2}, 20 keV/atom B_1 monomer and B_4 cluster ion implantations.

Condition	Peak	I_0 (counts)	FWHM (cm^{-1})
Non-implanted	LO	64173	10.8
B_1 implant	LO	2965[a]/57022[b]	15.7/11.0
	TO	2722/–	70.7/–
B_4 implant	LO	–/62803	–/10.9
	TO	3295/–	70.1/–

[a] As-implanted.
[b] As-annealed.

Fig. 2 illustrates the as-implanted (top) and as-annealed (bottom) Raman spectra for both the B_1 and B_4 implants. In essence, there are four Raman characteristic peaks of interest: (1) a sharp peak at approximately 520 cm^{-1} due to the longitudinal optical (LO) phonon in the crystalline silicon (c-Si) phase [22]; (2) a broad peak (or plateau) at approximately 960 cm^{-1} due to the second-order transverse optical (2TO) phonon in the c-Si phase [23]; (3) a sharp peak at approximately 305 cm^{-1} due to the second-order transverse acoustical (2TA) phonon in the c-Si phase [24]; and (4) a broad peak at approximately 470 cm^{-1} due to the transverse optical (TO) phonon in the amorphous silicon (a-Si) phase [25]. In this study, the LO and TO peaks are employed to represent the c-Si and a-Si phases, respectively, due to their primary significance.

Variations of LO and TO peaks in the as-implanted and as-annealed specimens for both the B_1 and B_4 implants are quantitatively investigated by fitting the TO and LO peaks to Gaussian and Lorentzian distributions, respectively. The peak parameters, including peak intensity (I_0) and full width at half maximum (FWHM), are listed in Table 1.

For the as-implanted specimens, as shown in Fig. 2, the appearance of both LO and TO peaks in the B_1 Raman spectrum in contrast to the appearance of essentially only a TO peak in the B_4 one indicates that the former contains a heavily-damaged structure while an amorphous layer exists in the latter. This phenomenon also reveals that a total atomic fluence of 2×10^{15} cm^{-2} is insufficient for the B_1 implantation to form an amorphous layer due mainly to the effects of *in situ* annealing and ion channeling. However, the B_4 implantation leads to high-density irradiation of incident atoms via local energy deposition and multiple collisions in the target material [6]. In addition, the overlapping damage even converts some temporary damage into permanent damage [26–28]. Hence, the non-linear damage effect caused by the B_4 implantation prevails the effects of *in situ* annealing and ion channeling and an amorphous layer thus results. In addition, as can be also seen in Table 1, a larger I_0 and smaller FWHM in the TO peak provides further evidence that the as-implanted B_4 specimen contains a greater amount of radiation damage compared to the as-implanted B_1 one.

For the as-annealed specimens, as shown in Fig. 2, both the B_1 and B_4 implantations illustrate the disappearance of the TO peak and the co-appearance of the LO, 2TO, and 2TA peaks. This phe-
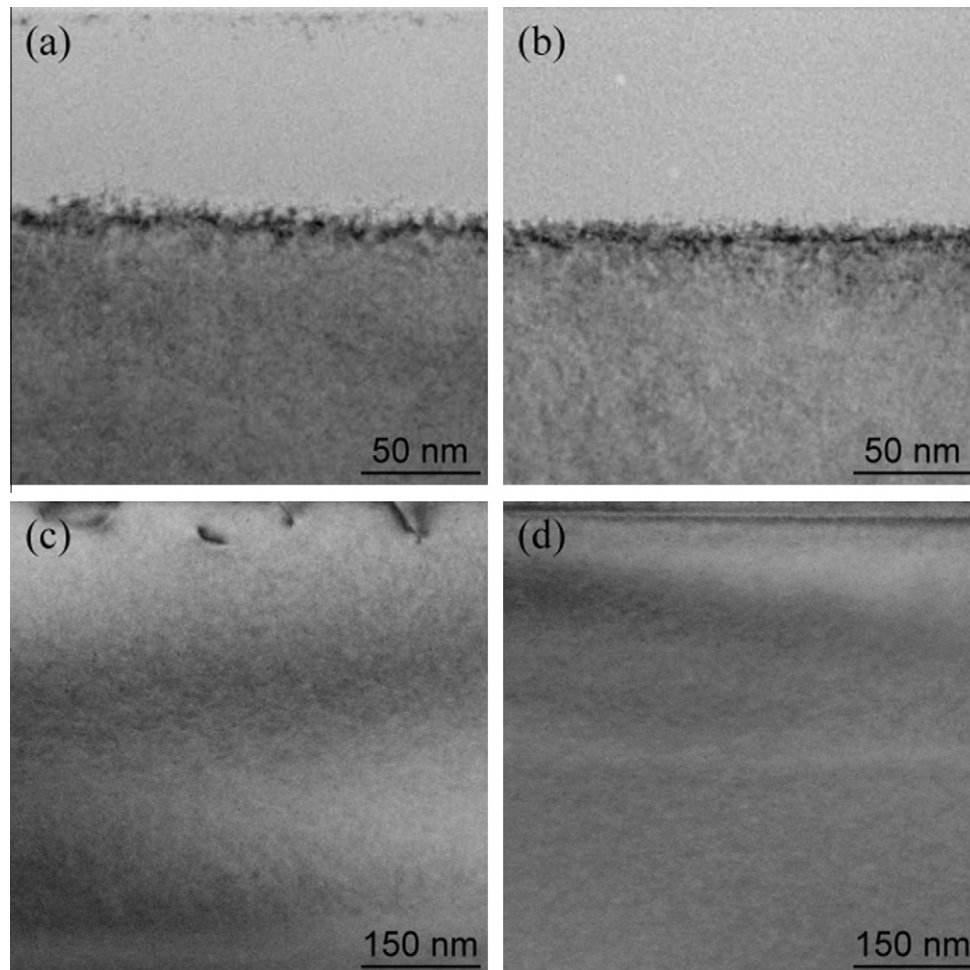

Fig. 3. XTEM images of the as-implanted (top) and as-annealed (bottom) specimens with 2×10^{15} cm^{-2}, 20 keV/atom B_1 monomer (left) and B_4 cluster (right) ion implantations.
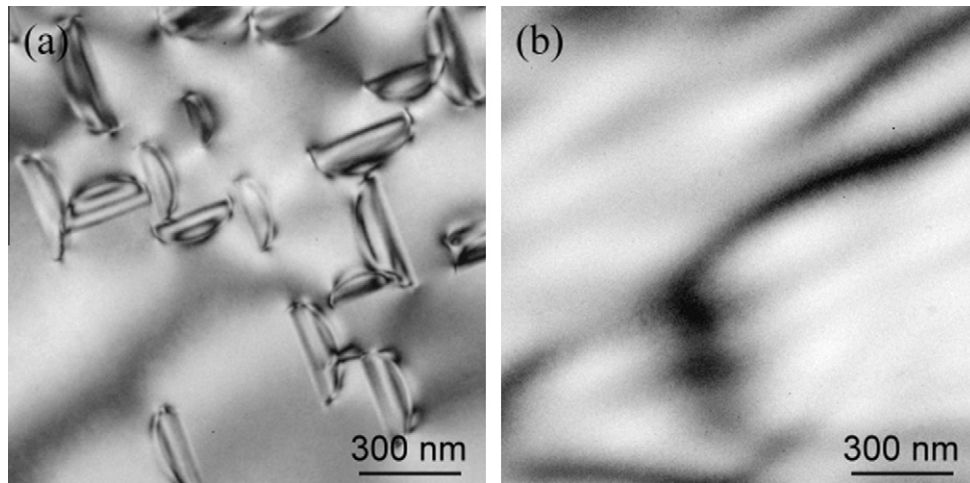
Fig. 4. PTEM images of the as-annealed specimens with 2×10^{15} cm^{-2}, 20 keV/atom B_1 monomer (left) and B_4 cluster (right) ion implantations.

nomenon indicates the disappearance of the amorphous structure together with the accompanying recovery of the crystalline structure. As can be also seen in Table 1, both the as-annealed B_1 and B_4 specimens have a larger I_0 and smaller FWHM in the LO peak compared to the as-implanted ones, indicating that annealing causes significant damage removal or crystalline recovery. Furthermore, the fact that solid phase epitaxial growth (SPEG) [3,13,29–31] is well-developed in the as-annealed B_4 specimen to more effectively remove radiation damage accounts for why the resultant LO peak has a larger I_0 and smaller FWHM compared to the as-annealed B_1 one. Also notice that the behaviors of the 2TA and 2TO peaks are quite similar to those of the LO peak, confirming again the phenomena mentioned above.

Fig. 3 displays the XTEM images for the as-implanted (top) and as-annealed (bottom) specimens due to B_1 and B_4 implants. The top of each image is the specimen surface. Fig. 3 (top) shows a great amount of radiation damage in both the as-implanted B_1 and B_4 specimens. In particular, the as-implanted B_1 specimen shows a heavily-damaged layer (86.0 nm) while an amorphous layer (91.4 nm) is apparent in the as-implanted B_4 one, corroborating the RSS results mentioned above. Also, the amorphous layer thickness obtained in the as-implanted B_4 specimen corresponds well to the SRIM-calculated one (90.8 nm). In other words, the additional radiation damage gained due to the non-linear damage effect in the B_4 implant counterweighs the radiation damage lost due to the effects of *in situ* annealing and ion channeling. In Fig. 3 (bottom), both the as-annealed B_1 and B_4 specimens show a great reduction of radiation damage. In particular, residual defects such as {3 1 1} defects and dislocation loops can be clearly seen in the as-annealed B_1 specimen while no such defects are visible in the as-annealed B_4 specimen. That is, the occurrence of SPEG in the as-annealed B_4 specimen during annealing eliminates a considerable amount of defects. Hence, residual damage in the as-annealed B_4 specimen is comparatively less than it is in the as-annealed B_1 one, confirming again the RSS results stated above.

The PTEM images for the as-annealed specimens due to B_1 and B_4 implants are depicted in Fig. 4. As can be seen, the topography of the as-annealed B_1 specimen clearly reveals spatially-separated dislocation loops and rod-like defects. However, in the as-annealed B_4 specimen, the topography is very clear and does not show any clear evidence of dislocation loops and rod-like defects. Notably, the dark bands existed in the image of the as-annealed B_4 specimen are due to thickness fringes and bend contours. It is also obvious that both the XTEM and PTEM results are in close correspondence.

4. Conclusions

The results of this study reveal that the characteristics of radiation damage induced by boron cluster ion implantation in silicon are strongly dependent on cluster size. In the Raman spectra, the appearance of an amorphous phase in the specimens can be clearly identified by a lower and wider longitudinal optical phonon Raman peak or a greater and narrower transverse optical phonon Raman peak. The opposite is true for the recovery of a crystalline phase. In essence, the non-linear damage effect is enhanced as cluster size increases. That is, the threshold ion fluence to initialize amorphization using B_4 cluster ion implantation is much less than that of B_1 monomer ion implantation. Also, the effects of *in situ* annealing and ion channeling tend to smooth out the damage depth profile and consequently increase the threshold ion fluence. Furthermore, the B_1 implant employed in this study only leads to a heavily-damaged layer in the as-implanted B_1 specimen. A band containing spatially-separated dislocation loops and rod-like defects is formed near the surface in the as-annealed B_1 specimen. However, the B_4 implant employed in this study produces a sufficiently-thick amorphous layer in the as-implanted B_4 specimen. The well development of SPEG when annealed at low temperatures (such as the FA step employed in this study) explains why radiation damage is substantially reduced and no visible defects can be found in the as-annealed B_4 specimen.

References

[1] National Technology Roadmap for Semiconductors, Semiconductor Industry Association, 1997 Edition, San Jose, CA, USA.
[2] X. Lu, L. Shao, X. Wang, J. Liu, W.-K. Chu, J. Bennett, L. Larson, P. Ling, J. Vac. Sci. Technol. B 20 (2002) 992.
[3] X. Lu, L. Shao, J. Jin, X. Wang, Q.Y. Chen, J. Liu, P. Ling, W.-K. Chu, Proceedings of the 16th International Conference on Application of Accelerators in Research and Industry, Denton, Texas, USA, November 1–4 (2000) p. 983.
[4] S. Moffatt, Nucl. Instr. and Meth. B 96 (1995) 1.
[5] T. Aoki, J. Matsuo, G. Takaoka, N. Toyoda, I. Yamada, Nucl. Instrum. Methods B 206 (2003) 855.
[6] D. Takeuchi, N. Shimada, J. Matsuo, I. Yamada, Nucl. Instrum. Methods B 121 (1997) 345.
[7] J.H. Liang, H.M. Han, Nucl. Instrum. Methods B 228 (2005) 250.

[8] J.H. Liang, H.M. Han, Nucl. Instrum. Methods B 249 (2006) 397.
[9] I. Yamada, G.H. Takaoka, M.I. Current, Y. Yamashita, M. Ishii, Nucl. Instrum. Methods B 74 (1993) 341.
[10] W.K. Chu, Y.P. Li, J.R. Liu, J.Z. Wu, S.C. Tidrow, N. Toyoda, J. Matsuo, I. Yamada, Appl. Phys. Lett. 72 (1998) 246.
[11] K.S. Jones, K. Moller, J. Chen, M. Puga-Lambers, B. Freer, J. Berstein, L. Rubin, J. Appl. Phys. 81 (1997) 6051.
[12] H.U. Jaeger, J. Appl. Phys. 78 (1995) 176.
[13] L. Csepregi, W.K. Chu, H. Mueller, J.W. Mayer, Radiat. Eff. 28 (1976) 277.
[14] H. Ryssel, I. Ruge, Ion Implantation, John Wiley & Sons Ltd., Chichester, 1986.
[15] C. Carter, M. Maszara, D.K. Sadana, G.A. Rozgonyi, J. Liu, J. Wortman, Appl. Phys. Lett. 44 (1984) 459.
[16] R.D. Goldberg, J.S. Williams, R.G. Elliman, Nucl. Instrum. Methods B 106 (1995) 242.
[17] M. Craig, A. Sultan, K. Reddy, B. Banerjee, E. Ishida, L. Larson, J. Vac. Sci. Technol. B14 (1996) 255.
[18] D.F. Downey, C.M. Osburn, J. Cummings, S.L. Daryanani, S. Falk, Thin Solid Films 308/309 (1997) 562.
[19] See http://www.jobinyvon.cn/cndivisions/raman.
[20] J.F. Ziegler, J.P. Biersack, U. Littmark, The Stopping and Range of Ions in Solids, vol. 1, Pergamon Press, New York, 1985.

[21] W. Eckstein, Computer Simulation of Ion-Solid Interactions, Springer, Berlin, 1991.
[22] V. Paillard, P. Puech, M.A. Laguna, R. Carles, B. Crales, B. Kohm, F. Huisken, Jpn. J. Appl. Phys. 86 (1999) 1921.
[23] K.P. Jain, A.K. Shukla, R. Ashokan, S.C. Abbi, M. Balkanski, Phys. Rev. B32 (1985) 6688.
[24] M. Takakura, T. Kinoshita, T. Uranishi, S. Miyazaki, M. Koyangi, M. Hirose, Jpn. J. Appl. Phys. 30 (1991) 3627.
[25] R. Albrn, D. Weaire, J.E. Smith, M.H. Brodski, Phys. Rev. B 11 (1975) 2271.
[26] J. Liu, X. Wang, L. Shao, X. Lu, W.-K. Chu, Nucl. Instrum. Methods B 190 (2002) 787.
[27] T. Aoki, T. Seki, J. Matsuo, Z. Insepov, I. Yamada, Nucl. Instrum. Methods B 153 (1999) 264.
[28] T. Aoki, T. Seki, M. Tanomure, J. Matsuo, I. Yamada, MRS Symp. Proc. 504 (1999) 93.
[29] L. Csepregi, E.F. Kennedy, T.J. Gallagher, J.W. Mayer, T.W. Sigmon, J. Appl. Phys. 48 (1977) 4234.
[30] E.F. Kennedy, L. Csepregi, J.W. Mayer, T.W. Sigmon, J. Appl. Phys. 48 (1977) 4241.
[31] J. Xu, E.G. Roth, O.W. Holland, A.P. Mills Jr., R. Suzuki, Appl. Phys. Lett. 74 (1999) 997.